

Continuous non-autonomous memristive Rulkov model with extreme multistability

Quan Xu(徐权), Tong Liu(刘通), Cheng-Tao Feng(冯成涛), Han Bao(包涵), Hua-Gan Wu(武花干), and Bo-Cheng Bao(包伯成)

Citation: Chin. Phys. B, 2021, 30 (**12**): 128702. DOI: 10.1088/1674-1056/ac2f30
Journal homepage: http://cpb.iphy.ac.cn; http://iopscience.iop.org/cpb

What follows is a list of articles you may be interested in

Computational model investigating the effect of magnetic field on neural-astrocyte microcircuit

Li-Cong Li(李利聪), Jin Zhou(周瑾), Hong-Ji Sun(孙洪吉), Peng Xiong(熊鹏), Hong-Rui Wang(王洪瑞), Xiu-Ling Liu(刘秀玲), and Chang-Yong Wang(王常勇)

Chin. Phys. B, 2021, 30 (**6**): 068702. DOI: 10.1088/1674-1056/abea81

Polarization conversion metasurface in terahertz region

Chen Zhou(周晨), Jiu-Sheng Li(李九生)

Chin. Phys. B, 2020, 29 (**7**): 078706. DOI: 10.1088/1674-1056/ab9295

Adjustable polarization-independent wide-incident-angle broadband far-infrared absorber

Jiu-Sheng Li(李九生), Xu-Sheng Chen(陈旭生)

Chin. Phys. B, 2020, 29 (**7**): 078703. DOI: 10.1088/1674-1056/ab8892

Effect of terahertz pulse on gene expression in human eye cells

Jin-Wu Zhao(赵晋武), Ming-Xia He(何明霞), Li-Jie Dong(东莉洁), Shao-Xian Li(李绍限), Li-Yuan Liu(刘立媛), Shao-Chong Bu(步绍翀), Chun-Mei Ouyang(欧阳春梅), Peng-Fei Wang(王鹏驰), Long-Ling Sun(孙珑玲)

Chin. Phys. B, 2019, 28 (**4**): 048703. DOI: 10.1088/1674-1056/28/4/048703

Avian magnetoreception model realized by coupling a magnetite-based mechanism with a radical-pair-based mechanism

Lü Yan, Song Tao

Chin. Phys. B, 2013, 22 (**4**): 048701. DOI: 10.1088/1674-1056/22/4/048701

SPECIAL TOPIC — Interdisciplinary physics: Complex network dynamics and emerging technologies

Continuous non-autonomous memristive Rulkov model with extreme multistability*

Quan Xu(徐权), Tong Liu(刘通), Cheng-Tao Feng(冯成涛), Han Bao(包涵), Hua-Gan Wu(武花干), and Bo-Cheng Bao(包伯成)†

School of Microelectronics and Control Engineering, Changzhou University, Changzhou 213164, *China*

(Received 15 July 2021; revised manuscript received 9 October 2021; accepted manuscript online 13 October 2021)

Based on the two-dimensional (2D) discrete Rulkov model that is used to describe neuron dynamics, this paper presents a continuous non-autonomous memristive Rulkov model. The effects of electromagnetic induction and external stimulus are simultaneously considered herein. The electromagnetic induction flow is imitated by the generated current from a flux-controlled memristor and the external stimulus is injected using a sinusoidal current. Thus, the presented model possesses a line equilibrium set evolving over the time. The equilibrium set and their stability distributions are numerically simulated and qualitatively analyzed. Afterwards, numerical simulations are executed to explore the dynamical behaviors associated to the electromagnetic induction, external stimulus, and initial conditions. Interestingly, the initial conditions dependent extreme multistability is elaborately disclosed in the continuous non-autonomous memristive Rulkov model. Furthermore, an analog circuit of the proposed model is implemented, upon which the hardware experiment is executed to verify the numerically simulated extreme multistability. The extreme multistability is numerically revealed and experimentally confirmed in this paper, which can widen the future engineering employment of the Rulkov model.

Keywords: extreme multistability, memristor, electromagnetic induction, Rulkov model

PACS: 87.50.−a, 87.19.ll, 87.23.Kg **DOI:** 10.1088/1674-1056/ac2f30

1. Introduction

The biological neurons play an essential role in electrical information dealing of nervous system.[1] Thus, it is important to disclose the dynamical prosperities of biological neurons in order to explore the mystery of nervous system. To date, diverse neuron models have been built to depict the main dynamical properties of neuron activities.[2] These neuron models can be mainly classified into two categories. One category is conductance-dependent neuron models, such as Hodgkin–Huxley model,[3] Morris–Lecar model,[4] Chay model,[5,6] and Wilson model,[7] which employs the electrophysiological characteristics of the cell membrane to reconstruct the ion channels to imitate the neuron activities. The other category is conductance-independent neuron models, i.e., Hindmarsh–Rose (HR) model,[8] FitzHugh–Nagumo model,[9] Izhikevich model,[10] and discrete Rulkov map,[11] which is constructed on dynamical assumptions to express the electrical activities of in- and out-signal without the consideration of neuron physiological structure. Most of these neuron models, no matter which categories they belong to, can generate rich electrical activities in response to externally applied stimulus,[12,13] electromagnetic induction,[14] and electromagnetic radiation.[15,16] That is to say, the neuron can realize its functions by feeling externally applied stimulus and conduction excitation of the change electrophysiology.[17,18]

To date, many explorations have revealed that externally applied stimulus and electromagnetic induction influence the dynamical properties of neuron electrical activities. By introducing an external applied current into HR model, various types of coexisting asymmetric bursters were disclosed.[12] And then, an external bipolar pulse current was imposed onto a two-dimensional (2D) HR model to imitate the periodic stimulus effect, from which the coexisting firing patterns have been explored.[13] Besides, the change of membrane potential during the exchange of intracellular ions and extracellular ions can lead to the variations of inner electrical field and induced current flow, and then a magnetic flow is induced.[19] Therefore, the effect of electromagnetic induction caused by the inner electrical field fluctuation should be considered in exploring the electrical activities of a neuron.[20] In other words, the electromagnetic induction participates and affects the electrical activity in a biological neuron. When modeling the neuron electrical activity with the consideration of electromagnetic induction effect, a flux-controlled memristor-enabled neuron model can be utilized for characterizing the electromagnetic induction effect.[21,22] The state equation of a flux-controlled memristor is restricted by the magnetic flux variation rate and applying voltage. Also, the memductance of a flux-controlled

*Project supported by the National Natural Science Foundation of China (Grant Nos. 12172066, 61801054, and 51777016), the Natural Science Foundation of Jiangsu Province, China (Grant No. BK20160282), and the Postgraduate Research and Practice Innovation Program of Jiangsu Province, China (Grant No. KYCX21_2823).

†Corresponding author. E-mail: mervinbao@126.com

© 2021 Chinese Physical Society and IOP Publishing Ltd

memristor is really dependent on its crossing flux.[23,24] These constraint relations of the flux-controlled memristor can effectively imitate the interaction between the electromagnetic induction effect and membrane potential of a biological neuron. Employing this scheme, many fascinating memristive neuron models have been raised and abundant electrical activities were numerically revealed.[25–28]

Inspired by the pioneer work, dynamical responses with different firing patterns and stochastic resonance were observed in the Hodgkin–Huxley neuron model by employing a flux-controlled memristor to emulate the electromagnetic induction flow.[29] The electromagnetic induction effects on the regulation of sleep wake cycle were further studied in a simple wake-sleep neural network coupled by glutamate synapse. It was found that the average firing frequency can be modified by the intensity of the electromagnetic induction.[30] And then, with comprehensive considerations of the electromagnetic induction and radiation, high and low frequency stimulus, and Gaussian white noise, mode transition of electrical activities and thought-provoking phenomena have been explored by bifurcation analysis.[31] To further reveal the effectiveness of electromagnetic treatment of mental diseases, the regulatory abilities of external electromagnetic stimulus on the dynamical properties of a small-world Newman–Watts network were explored.[32] Specially, the coexistence of spiking and bursting behaviors in a Leech neuron model was revealed and the synchronization of the two behaviors was investigated by coupling two identical Leech neurons.[33] After that, to mimic the threshold effect of electromagnetic induction, a threshold flux-controlled memristor-based HR neuron model was considered, from which the coexisting hidden bursting patterns were disclosed.[34] By building a locally memristive neuron model, the multistbility phenomenon was numerically simulated and experimentally captured.[35] The multistbility with multiple firing patterns was also disclosed in neural network coupled by memristive synapse, within which the memristor was utilized to express the electromagnetic induction induced by the difference of membrane potentials.[36–38]

The phenomenon of multistability has attractive great attention due to its potential use in the applications of image processing tasks.[33] Multistability involves various kinds of coexisting attractors for different initial conditions under fixed system parameters.[24,39] It is not easy to theoretically predict the multistability, but the initial condition offset-boosting and adoption of an ideal memristor are two empirical methods for acquiring multistability.[40,41] In general, multistability has been frequently found in autonomous systems, but has been rarely reported in non-autonomous one.[42] In this paper, by considering an externally injected alternating current and memristive electromagnetic induction effect, a continuous non-autonomous memristive Rulkov model is built. The phenomenon of extreme multistability is discovered in numerical and experimental surveys of the proposed model, which has not been reported in the state-of-the-art.

The two-dimensional (2D) discrete map-based Rulkov model was firstly established to imitate the dynamical properties of spiking and bursting firing patterns of a real biological neuron.[43] Then, numerous literatures have been published to numerically disclose the dynamical properties with different considerations.[44–47] The occurrence of multiple bifurcations was revealed in a non-chaotic Rulkov map with the consideration of delay.[44] Thereafter, coherence resonance and stochastic spiking-bursting excitability in the 2D Rulkov model with noise[45,46] and random force were numerically disclosed.[47] Beyond the work of single Rulkov neuron, Rulkov neuron-based networks with electrical and chemical synapse were built, from which the stability and chaos evolution,[48] synchronization of two identical and non-identical Rulkov models,[49] and rich bursting patterns were numerically investigated.[50,51] All of these literatures were carried out in the numerical survey, but hardware implementation is more important for engineering application. Hardware implementation platforms can be divided into two categories, namely, analog hardware platform and digital hardware platform. Relatively speaking, analog hardware is one of the available way for the integrated circuit (IC) design,[52,53] which may promote a great convenience to engineering application of Rulkov model. Thus, a continuous Rulkov model is derived from the 2D map-based Rulkov model in this paper. Then, a continuous non-autonomous memristive Rulkov model is built by considering memristive electromagnetic induction and external stimulus. The electromagnetic induction flow is imitated by the generated current from a flux-controlled memristor and the external stimulus is injected using a sinusoidal current. The proposed Rulkov model can generate the novel phenomenon of extreme multistability with coexisting infinite firing patterns. The coexisting firing patterns in the proposed model can actually demonstrate multi-stable firing patterns emerging in biological neurons under the physical electrophysiological environment.

The remaining of this paper is arranged as follows. The continuous Rulkov model with the considerations of electromagnetic induction and external stimulus is built, and then the stability of the equilibrium point is numerically disclosed in Section 2. Parameter-associated dynamical behaviors are comprehensively explored in Section 3. Then, the extreme multistability depending on the initial conditions is further revealed in Section 4. Furthermore, the analog circuit-based hardware implementation and experimental measurement are executed in Section 5. Finally, the conclusion is drawn.

2. Model and equilibrium point stability

The 2D discrete map-based Rulkov model with a simple algebraic structure was firstly raised on dynamical assumptions of biological neurons.[43] It can reproduce periodic and chaotic spiking/bursting behaviors in biological neurons. Actually, a continuous nonlinear model is more efficient to reflect the dynamical property of a biological neuron due to its continuously dynamical evolution process. Thus, a continuous nonlinear model is derived by referring to the 2D discrete map-based Rulkov model. It can be mathematically written as

$$\begin{cases} \dfrac{\mathrm{d}x}{\mathrm{d}\tau} = \dfrac{\alpha}{1+x^2} - x + y, \\ \dfrac{\mathrm{d}y}{\mathrm{d}\tau} = -\sigma x - \beta, \end{cases} \tag{1}$$

where x represents the membrane potential and y stands for the gating process. α, β, and σ are three control parameters. Specially, σ is employed to control the changing rate of the gating process and β is an externally applied influence.

Model (1) can only generate periodic behavior, because it is a 2D autonomous nonlinear model, i.e., for $\alpha = 11$, $\sigma = \beta = 0.01$, and initial conditions $(x_0, y_0) = (0,0)$, model (1) generates a periodic spiking firing pattern. The phase trajectory and spiking firing pattern of the membrane potential x are numerically simulated as shown in Fig. 1. To exhibit its chaotic dynamics and to characterize the electrophysiology effects in the continuous Rulkov model, a continuous non-autonomous memristive Rulkov model is then built to address these issues.

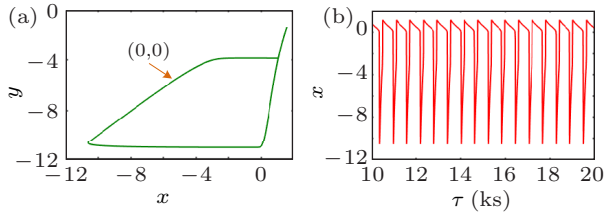


Fig. 1. (a) Phase trajectory and (b) spiking firing pattern of the membrane potential x for $\alpha = 11$, $\sigma = \beta = 0.01$, and initial conditions $(x_0, y_0) = (0,0)$.

Herein, a flux-controlled memristor with quadratic memductance $W(\varphi) = a + b\varphi^2$ is employed to characterize the electromagnetic induction when neural activities are triggered.[34] Thus, with the simultaneous consideration of externally injected sinusoidal current and electromagnetic induction, a continuous non-autonomous memristive Rulkov model is built and written as

$$\begin{cases} \dfrac{\mathrm{d}x}{\mathrm{d}\tau} = \dfrac{\alpha}{1+x^2} - x + y + A\sin(2\pi F\tau) + k(a+b\varphi^2)x, \\ \dfrac{\mathrm{d}y}{\mathrm{d}\tau} = -\sigma x - \beta, \\ \dfrac{\mathrm{d}\varphi}{\mathrm{d}\tau} = x, \end{cases} \tag{2}$$

where φ is the memristor inner state, $k(a+b\varphi^2)x$ stands for the electromagnetic induction flow, and k indicates the coupling strength of the electromagnetic induction. $A\sin(2\pi F\tau)$ is the externally injected sinusoidal current, in which A and F are the amplitude and frequency, respectively. The effects of electromagnetic induction and external stimulus are simultaneously considered herein, which have been rarely involved in the literature.

When $\beta = 0$, model (2) possesses a line equilibrium set of $\boldsymbol{E} = (\bar{x}, \bar{y}, \bar{\varphi}) = (0, -\alpha - A\sin(2\pi F\tau), c)$, within which c has an arbitrary real value. Whereas, model (2) has no equilibrium point for $\beta \neq 0$, which induces that model (2) generates hidden dynamics.[42] By numerous numerical simulations, it is found that model (2) generates transient periodic/chaotic behaviors but then tends to infinite in this case.[54] Thus, we mainly concern on the case of $\beta = 0$ and select typical model parameters as $\alpha = 11$, $\sigma = 6$, $A = 2$, $F = 1$, $a = 1$, $b = 2$, and $k = 0.1$.

By linearizing model (2) around any equilibrium point of $\boldsymbol{E}$, the Jacobian matrix is obtained as

$$\boldsymbol{J}_{\boldsymbol{E}} = \begin{bmatrix} \dfrac{-2\alpha\bar{x}}{(1+\bar{x}^2)^2} - 1 + k(a+b\bar{\varphi}^2) & 1 & 2kb\bar{\varphi}\bar{x} \\ -\sigma & 0 & 0 \\ 1 & 0 & 0 \end{bmatrix}. \tag{3}$$

At the line equilibrium set $\boldsymbol{E}$, the characteristic equation can be deduced as

$$\begin{aligned} \det(\mathbf{1}\lambda - \boldsymbol{J}_{\boldsymbol{E}}) &= \lambda\{\lambda^2 + [1 - k(a+bc^2)]\lambda + \sigma\} \\ &= 0. \end{aligned} \tag{4}$$

Model (2) has a line equilibrium set evolving over the time. For the selected typical model parameters, the line equilibrium set is plotted in Fig. 2(a). Note that the value of $\bar{\varphi}$ for the line equilibrium set is infinite and only illustrated in the region $[-6, 6]$. Besides, the characteristic equation (4) has one zero eigenvalue and two nonzero eigenvalues. The stability of the line equilibrium set is really restricted by the model parameters a, b, σ, k, and the arbitrary real value c. When c is increased from -6 to 6 and parameter k is changed from 0 to 0.5 with other parameters fixed, the stability distribution of the line equilibrium set in the c–k plane is figured out in Fig. 2(b). The region I colored in blue has two positive real roots and the region II colored in yellow has a pair of complex conjugate roots with positive real parts. Different from these two regions, the region III colored in grey has a pair of complex conjugate roots with negative real parts. Summarily, I and II are two unstable regions, and III is stable region. Thus, model (2) can give birth to rich dynamics with the variations of parameters c and k.

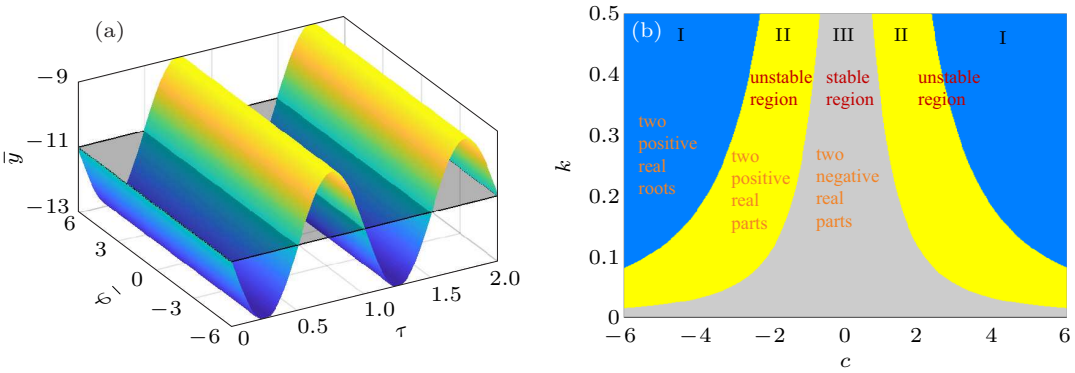


Fig. 2. Line equilibrium set and stability distributions for $\alpha = 11$, $\sigma = 6$, $A = 2$, $F = 1$, $a = 1$, $b = 2$. (a) Line equilibrium set evolving over the time; (b) stability distributions restricted to the two nonzero eigenvalues in the c–k plane.

3. Parameter-associated dynamical behaviors

In this section, we select the model parameters k, α, A, and F as adjustable variables to explore the parameter-associated dynamical behaviors in model (2) numerically, where MATLAB-based ODE23 algorithm with fixed time step 0.01 s and time interval [1.5 ks, 2 ks] is used in plotting one-dimensional (1D) and two-dimensional (2D) bifurcation diagrams. Besides, Wolf's Jacobi method[55] with fixed time step 0.1 s and total time 10 ks is employed in depicting Lyapunov exponents and dynamical map. The initial conditions $(x, y, \varphi) = (0, 0, 0)$ are assigned.

3.1. Parameters k and α related numerical plots

In this subsection, the dynamical behavior is fully disclosed by 2D bifurcation diagram depicted by checking the periodicities of the membrane potential x and dynamical map described by the largest Lyapunov exponent in the k–α parameter plane as illustrated in Fig. 3.

In Fig. 3(a), the colormap is utilized to distinguish different dynamical behaviors, on which the red color labeled by CH denotes chaotic behaviors. The grey color labeled by UB denotes the unbounded behavior and the other colors labeled by P01–P08 represent the periodic behaviors with different periodicities of period-1 to period-8. Whereas in Fig. 3(b), the different colors on the colormap represent the values of the largest Lyapunov exponent, among which the deep red to white colors with the positive largest Lyapunov exponent denote chaotic behaviors, the black ones with the negative values present the periodic behaviors, and the grey color denotes the unbounded behavior. These numerical simulations explicitly disclose that the complex dynamics demonstrated by the 2D bifurcation diagram in Fig. 3(a) well match those revealed by the dynamical map in Fig. 3(b). These confirm the occurrence of complex dynamical behaviors in the continuous non-autonomous memristive Rulkov model (2) with the variations of the model parameters k and α. Note that model (2) goes to infinite with large model parameter α and strong electromagnetic induction of large coupling strength.

To more clearly reveal the dynamical evolution, the 1D bifurcation diagram and finite-time Lyapunov exponent are numerically simulated as shown in Fig. 4. Here, only the largest Lyapunov exponent is illustrated. Model (2) shows periodic and chaotic behaviors with the variations of parameters k and α, and these dynamical behaviors are confirmed by the corresponding finite-time Lyapunov exponents, respectively. Note that the finite-time Lyapunov exponents do not exist while model (2) running in unbounded behavior with $k > 0.3625$ as shown in Fig. 4(b). The 1D bifurcation diagrams and finite-time Lyapunov exponent further confirm the complex dynamics in model (2).

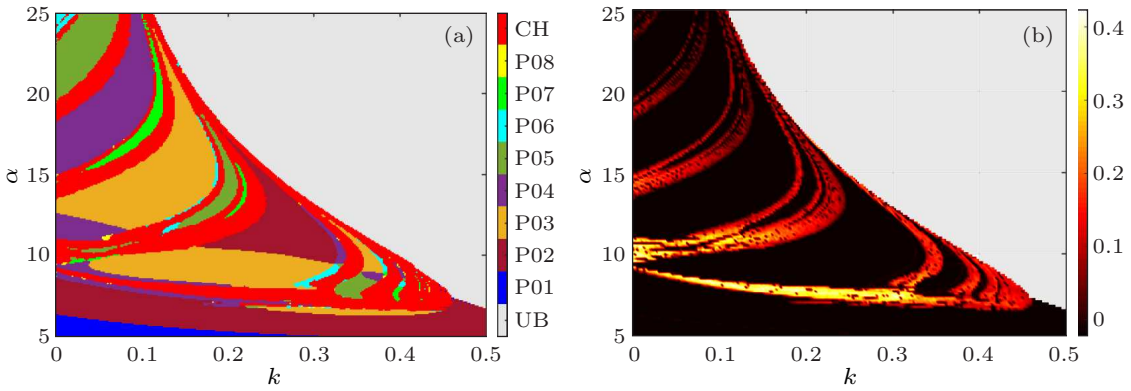


Fig. 3. The 2D plots in k–α parameter plane with $\sigma = 6$, $A = 2$, $F = 1$, $a = 1$, $b = 2$. (a) 2D bifurcation diagram; (b) dynamical map.

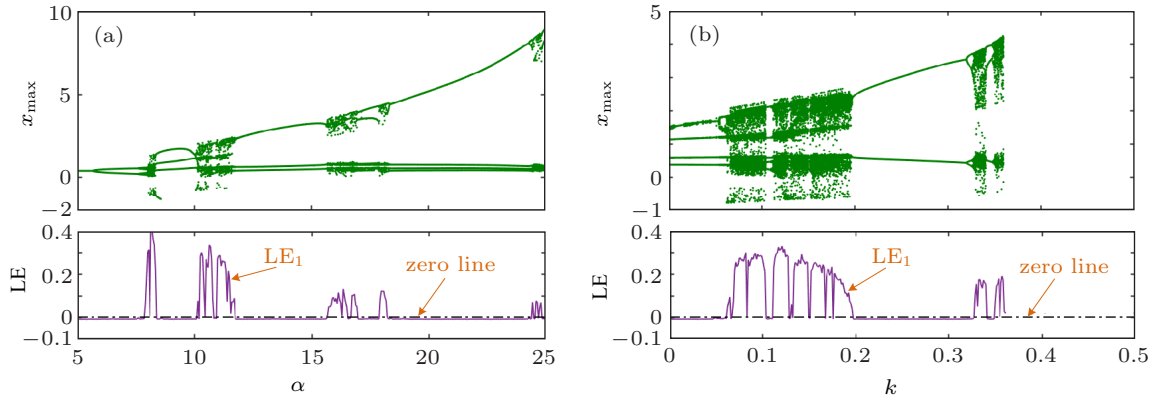


Fig. 4. The 1D bifurcation diagrams (up) and largest Lyapunov exponent (bottom) with the changes of (a) α and (b) k.

3.2. External stimulus related numerical plots

To disclose the dynamical behavior associated to the externally injected stimulus, we consider the stimulus related parameters A and F as two adjustable parameters while other parameters are taken as the typical ones. The 2D bifurcation diagram and dynamical map in the A–F parameter plane are depicted in Fig. 5. It is revealed that model (2) can generate rich dynamics with the changes of external stimulus related parameters. These reflect that the dynamical behaviors depend decisively on the externally injected stimulus. This can assistant us to understand the phenomenon of rapid mode transition under external stimulus in biological neuron. The dynamical behaviors revealed by 2D bifurcation diagram are basically coined with these disclosed by dynamical map. Note that model (2) tends to stable point attractor under small values of A and F parameter region. The narrow parameter region locates at the left-down with white color in the 2D bifurcation diagram.

Similarly, to more clearly reveal the dynamical evolution with respect to the external stimulus, the 1D bifurcation diagram and finite-time Lyapunov exponent are numerically simulated as A and F are changed respectively, as shown in Fig. 6. Model (2) shows periodic and chaotic behaviors with the variations of parameters A and F, and these dynamical behaviors are confirmed by the finite-time Lyapunov exponents, respectively. The 1D bifurcation plots further reveal the stimulus related complex dynamical behaviors in model (2).

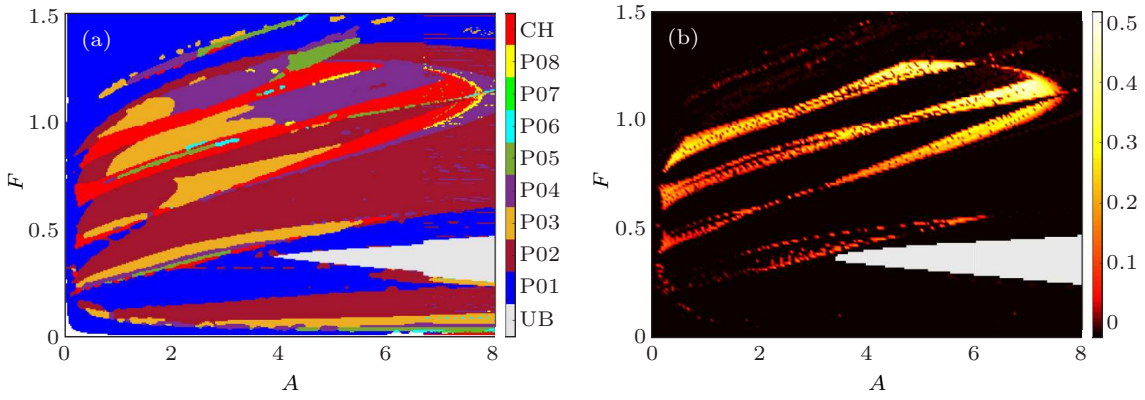


Fig. 5. The 2D plots in A–F parameter plane with $\alpha = 11$, $\sigma = 6$, $k = 0.2$, $a = 1$, $b = 2$. (a) 2D bifurcation diagram; (b) dynamical map.

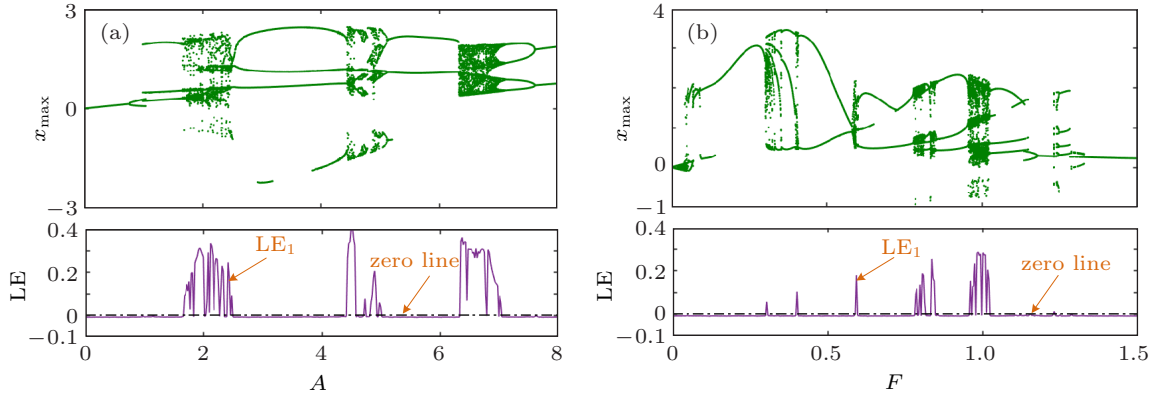


Fig. 6. The 1D bifurcation diagrams (up) and largest Lyapunov exponent (bottom) with the variations of (a) A and (b) F.

4. Initial condition-associated extreme multistability

As a special kind of multistability, the phenomenon of extreme multistability happens with the number of coexisting attractors going to infinity. This special phenomenon has been first found in a memristive Chua's circuit.[56] Then, initial-boosted extreme multistability in a two-memristor-based system[57] and hidden extreme multistability in a 5D system[58] have been revealed. In general, extreme multistability emerges in a system having an initial condition-associated perfect period-doubling bifurcation behavior. In this section, we mainly concern the initial condition-associated extreme multistability in model (2). The numerical simulations and colormap settings are identical with those utilized in Section 3.

4.1. Local attraction basin and dynamical map

The local attraction basins and dynamical maps in φ_0–y_0 and φ_0–x_0 initial condition planes are depicted in Figs. 7 and 8, respectively, which reveal that model (2) can generate rich initial condition-associated dynamical behaviors. The dynamical behaviors revealed by local attraction basin well coincide with these disclosed by dynamical maps. It is noted that the local attraction basin has the feature of inerratic strip structures.[59] This prominent feature implies that model (2) can easily generate a period-doubling bifurcation route by setting appropriate model parameters and initial conditions. The initial condition-associated period-doubling bifurcation route means the existence of extreme multistability, which indicates that model (2) can generate coexisting infinite firing patterns under the set of fixed model parameters. But the dynamical behavior does not alter with the initial condition x_0 along with the initial condition φ_0 unchanging, as shown in Fig. 8.

4.2. The 1D bifurcation plots

As predicted in Figs. 7 and 8, extreme multistability and coexisting infinite firing patterns can be induced by taming the initial conditions y_0 and φ_0. For better understanding, the 1D bifurcation plots are depicted in Fig. 9. The initial conditions $(0, y_0, 0)$ and $(0, 0, \varphi_0)$ are employed in checking the extreme multistability with respect to y_0 and φ_0, respectively. In Fig. 9(a), when the initial condition y_0 increases from -2, the trajectory of model (2) begins with chaotic behavior. Then tangent bifurcation happens at $y_0 = 0.158$, the trajectory runs into periodic behavior with period-5. Afterward, period-doubling bifurcation scenarios occur, the trajectory runs into chaotic behavior. The chaotic behavior extends to $y_0 = 1.484$ and then tangent bifurcation happens again, the trajectory falls into periodic behavior. Thereafter, the period-doubling bifurcation scenarios occur again, leading model (2) to run in chaotic behavior.

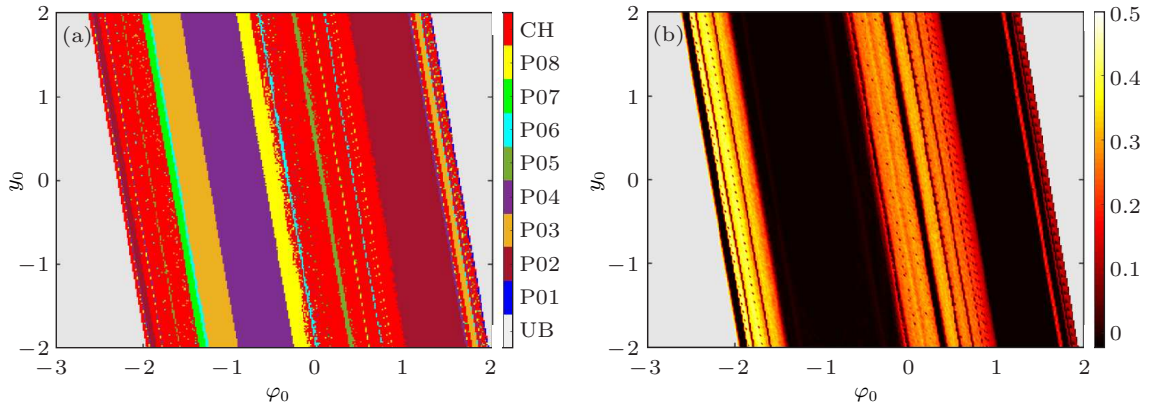


Fig. 7. The 2D plots in φ_0–y_0 initial condition plane under the typical model parameters. (a) Local attraction basin; (b) dynamical map.

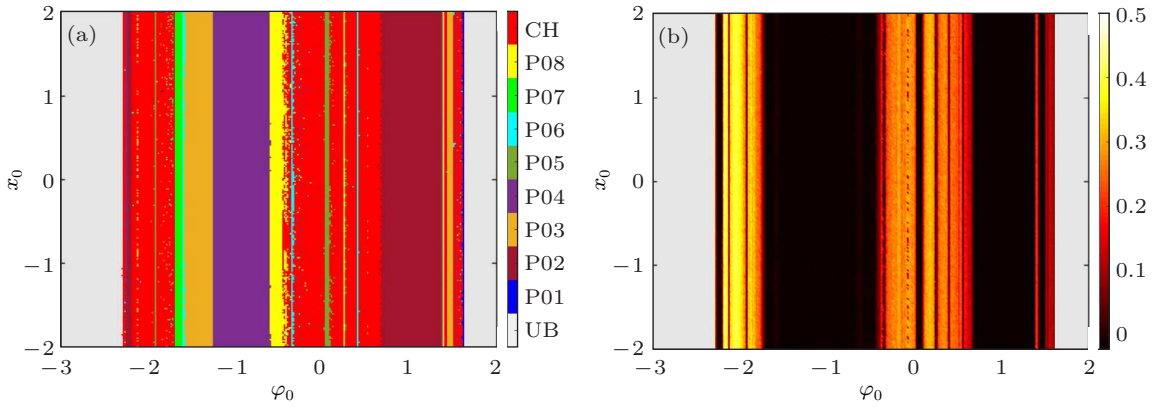


Fig. 8. The 2D plots in φ_0–x_0 initial condition plane under the typical model parameters. (a) Local attraction basin; (b) dynamical map.

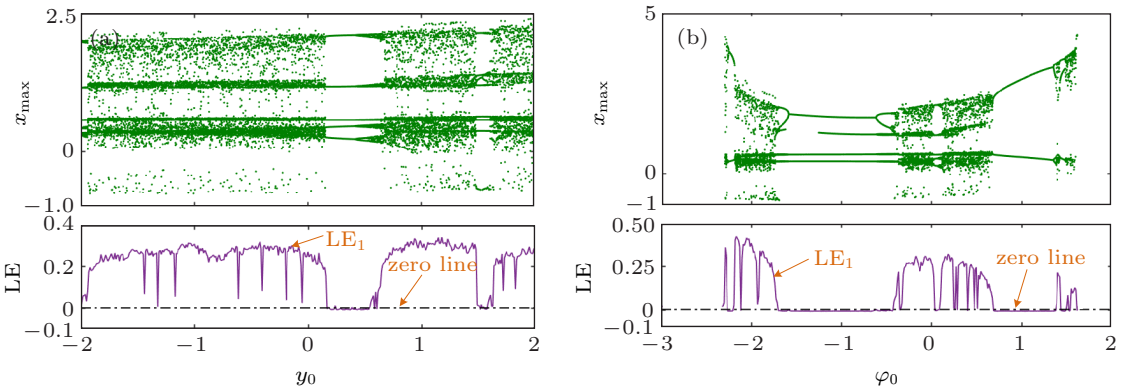


Fig. 9. The 1D bifurcation diagrams (up) and finite-time Lyapunov exponent (bottom) with the variations of (a) y_0 and (b) φ_0.

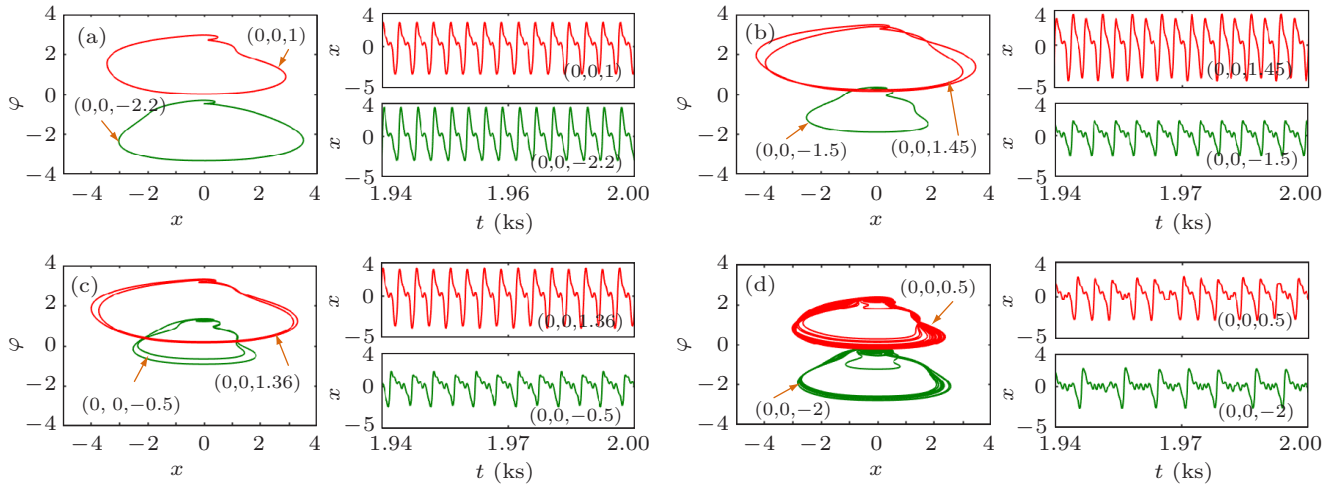


Fig. 10. Phase trajectories (left) and time-domain waveforms (right) for different initial condition φ_0. (a) Coexisting period-2 firing patterns for -2.2 and 1; (b) coexisting period-3 firing patterns for -1.5 and 1.45; (c) coexisting period-4 firing patterns for -0.5 and 1.36; (d) coexisting chaotic firing patterns for -2 and 0.5.

In Fig. 9(b), as the initial condition φ_0 increases from -3, the trajectory tends to infinite of unbounded behavior, then runs in chaotic behavior at $\varphi_0 = -2.295$. Afterwards, the trajectory declines into periodic behaviors via period-doubling bifurcations. Thereafter, chaotic crisis happens at $\varphi_0 = -2.183$, then the trajectory runs in chaotic behavior. The chaotic behavior extends to $\varphi_0 = -1.705$ and then the reverse period-doubling bifurcation scenarios occur, leading the model (2) to run in periodic behavior with period-3. After that, period-doubling bifurcation scenarios happen three times at $\varphi_0 = -0.618$, 0.070, and 1.355, and tangent bifurcations happen two times at $\varphi_0 = 0.028$ and 0.675, leading to that model (2) runs into periodic behaviors and chaotic behaviors alternately. Lastly, the trajectory tends to infinite of unbounded behavior at $\varphi_0 = 1.605$. Clearly, extreme multistability and coexisting infinite firing patterns associated to the initial conditions y_0 and φ_0 are further confirmed by the 1D bifurcation diagrams and finite-time Lyapunov exponents as shown in Fig. 9.

4.3. Phase trajectory and time-domain waveform

The phase trajectories and time-domain waveforms for some discrete values of initial condition φ_0 are plotted to further illustrate the extreme multistability with coexisting infinite firing patterns, as shown in Fig. 10. Here, the fixed time step 0.01 s and time interval [1.9 ks, 2 ks] are employing in plotting the phase trajectory. The time interval [1.94 ks, 2 ks] is employed in plotting time-domain waveform for more clearly visualization. The phase trajectories and time-domain waveforms for different initial condition φ_0 are illustrated in Figs. 10(a)–10(d) respectively. It is revealed that the proposed model (2) can truly generate coexisting periodic and chaotic firing patterns. Actually, the firing patterns are non-standard spiking and bursting firing patterns. This reflect that the simultaneously considered electromagnetic induction and external stimulus can exert an influence on the dynamical properties of biological neurons.

5. Circuit implementation and experimental verification

The analog circuit implementation can involve the physical effects of parasitic circuit parameters for electronic neuron. Thus, the electronic neurons in analog form are significant to develop applications in artificial neural networks.[60] The model (2) can be equivalently realized by analog circuit.[1]

The schematic of the equivalent circuit is given in Fig. 11, the circuit equations for the three capacitor voltages V_x, V_y, and V_φ are modeled as

$$\begin{cases} RC\dfrac{\mathrm{d}V_x}{\mathrm{d}t} = \dfrac{R}{R_4}\dfrac{V_2}{g_4\Big(-\dfrac{R_{12}}{R_{11}}V_1+\dfrac{R_{12}}{R_{10}}g_3V_x^2\Big)} - \dfrac{R}{R_7}V_x \\ \qquad\qquad + \dfrac{R}{R_6}V_y + \dfrac{R}{R_5}V_{\mathrm{S}} + \Big(\dfrac{R}{R_2}+\dfrac{g_1g_2R}{R_3}V_\varphi^2\Big)V_x, \\ RC\dfrac{\mathrm{d}V_y}{\mathrm{d}t} = -\dfrac{R}{R_{16}}V_x, \\ RC\dfrac{\mathrm{d}V_\varphi}{\mathrm{d}t} = \dfrac{R}{R_1}V_x, \end{cases} \tag{5}$$

where $V_{\mathrm{S}} = V_{\mathrm{m}}\sin(2\pi ft)$ is the input voltage to equivalently represent the externally injected current with the expression of V_{S}/R_5, V_1, V_2 are two direct voltages, and g_1, g_2, g_3, and g_4 are the gains of the four multipliers M_1, M_2, M_3, and M_4, respectively. $t = RC\tau$ is the physical time and RC is the integral time constant.

Since the dynamic range of the state variable V_y exceeds the normal operation ranges of the active devices in Fig. 11, i.e., operational amplifier AD711JN and multiplier AD633JN, a linear transformation should be made for decreasing the dynamic range of V_y in Eq. (5) as

$$(V_x, V_y, V_\varphi) \to (V_x, 7V_y, V_\varphi). \tag{6}$$

Therefore, substituting Eq. (6) into Eq. (5) and comparing Eq. (5) with Eq. (2), as well as supposing $V_1 = -1$ V and $V_2 = 1$ V, it yields

$$\begin{aligned} R_1 &= R_5 = R_7 = R_8 = R_9 = R_{10} = R_{11} = R_{12} \\ &= R_{13} = R_{14} = R_{15} = R_{17} = R_{18} = R, \\ R_2 &= \frac{R}{ka},\ R_3 = \frac{g_1g_2R}{kb},\ R_4 = \frac{R}{\alpha},\ R_6 = \frac{R}{7}, \\ R_{16} &= \frac{7R}{\sigma},\ V_{\mathrm{m}} = A,\ f = \frac{F}{RC}. \end{aligned} \tag{7}$$

Suppose the integral time constant $RC = 0.1$ ms (i.e., $R = 10$ kΩ and $C = 10$ nF) and $g_1 = g_2 = g_3 = g_4 = 1$, the circuit parameters for the typical model parameters are calculated as $R_1 = R_5 = R_7 = R_8 = R_9 = R_{10} = R_{11} = R_{12} = R_{13} = R_{14} = R_{15} = R_{17} = R_{18} = 10$ kΩ, $R_2 = 100$ kΩ, $R_3 = 50$ kΩ, $R_4 = 0.909$ kΩ, $R_6 = 1.428$ kΩ, $R_{16} = 11.667$ kΩ, $V_{\mathrm{m}} = 2$ V, and $f = 10$ kHz.

Refering to the circuit schematic in Fig. 11, an analog circuit is manually welded by commercially available discrete components on a printed circuit board. The monolithic capacitors and precise potentiometers, as well as the operational amplifiers AD711JN and multipliers AD633JN with ±15 V voltage supplies are employed. The experimental results are captured by a Tektronix TDS 3054C digital oscilloscope in XY mode. To confirm the coexisting infinite firing patterns in the hardware experiment, the circuit parameters corresponding to the typical model parameters are employed. Only the resistance R_4 in the analog circuit is adjusted to fine tune the hardware circuit. It is noted that the desired initial capacitor voltages are difficult to accurately acquire in the hardware circuit, which are randomly sensed through repeatedly turning on and off the hardware circuit power supplies.[24,36] The experimental resistance $R_4 = 0.752$ kΩ, which is different from the theoritcal value $R_4 = 0.909$ kΩ. This deviation is

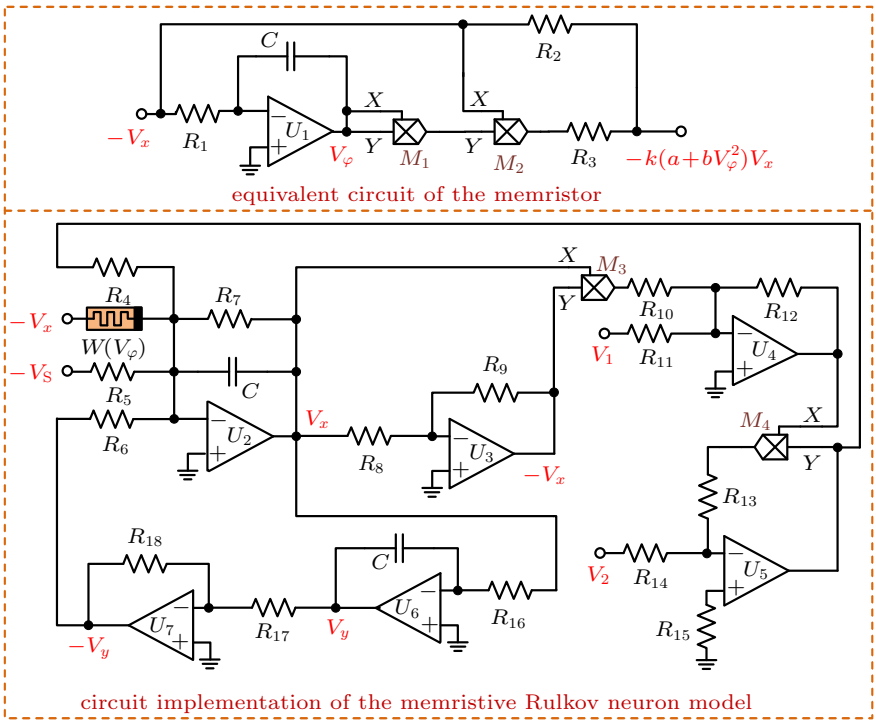


Fig. 11. Equivalent circuit implementations of the continuous non-autonomous memristive Rulkov model (bottom) and the memristor (up).

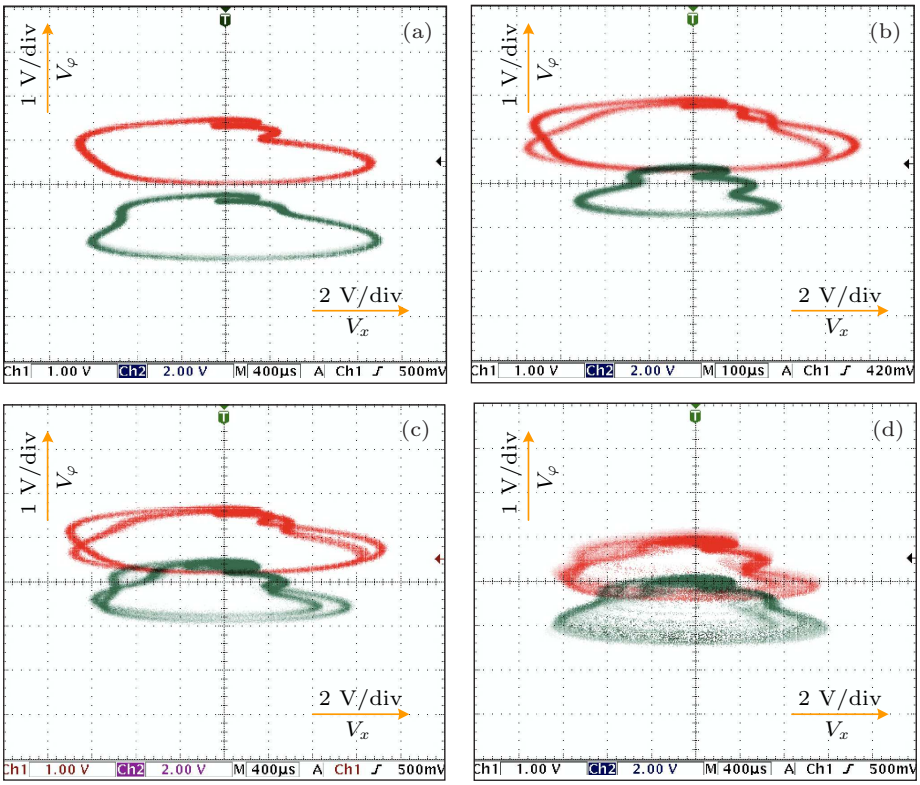


Fig. 12. Experimentally captured phase trajectories for random sensed initial conditions. (a) Coexisting period-2 firing patterns; (b) coexisting period-3 firing patterns; (c) coexisting period-4 firing patterns; (d) coexisting chaotic firing patterns.

caused by the model idealizations, parasitic parameters, measurement errors, and so on. Corresponding to the phase trajectories in Fig. 10, the coexisting infinite firing patterns are experimentally captured, as illustrated in Fig. 12. Besides, Fig. 12 displays eight kinds of coexisting attractors for a fixed set of circuit parameters. For observability and to save space, these coexisting attractors are combined on the four figures by Photoshop processing.

6. Conclusions

In this paper, a continuous Rulkov model was firstly derived from the 2D discrete map-based Rulkov model, and then a continuous non-autonomous memristive Rulkov model was constructed by taking into account the memristive electromagnetic induction and externally injected sinusoidal current. Thus, the proposed model possesses a time-varying line equilibrium set. The time-varying line equilibrium set and their stability distributions were numerically simulated. It was specially revealed that the stability of the line equilibria set is not only dependent on the model parameters but also associated to the initial location of the memristor. These features can result in the generations of rich dynamical behaviors and extreme multistability. Multiple numerical methods were employed to disclose the dynamical behavior in the Rulkov model, which revealed the generation of chaotic behavior and periodic behavior with different periodicities, as well as rich mode transition behaviors. Besides, the extreme multistability with coexisting infinitely firing patterns was numerically explored. These numerical explorations reflect that the memristive electromagnetic induction and external stimulus can trigger rich neuron dynamics in biological neuron. Moreover, analog circuit-based hardware experiments were executed, from which the phase trajectories were captured to verify the numerical simulations. Particularly, the simultaneously considered electromagnetic induction and external stimulus can lead to the occurrence of non-standard spiking and bursting firing patterns, which can better mirror the electrophysiological activities of biological neurons in complex electrophysiological environment.

References

[1] Yao Z, Zhou P, Zhu Z G and Ma J 2021 *Neurocomputing* **423** 518
[2] Xu L F, Li C D and Chen L 2016 *Acta Phys. Sin.* **65** 240701 (in Chinese)
[3] Hodgkin A L and Huxley A F 1952 *J. Physiol.* **117** 500
[4] Morris C and Lecar H 1981 *Biophys. J.* **35** 193
[5] Chay T R 1985 *Physica D* **16** 233
[6] Xu Q, Tan X, Zhu D, Bao H, Hu Y H and Bao B C 2020 *Chaos Solitons Fractals* **141** 110353
[7] Wilson H R 1999 *J. Theor. Biol.* **200** 375
[8] Hindmarsh J L and Rose R M 1982 *Nature* **296** 162
[9] FitzHugh R 1961 *Biophys. J.* **1** 445
[10] Izhikevich E M 1999 *IEEE Trans. Neural Netw.* **10** 499
[11] Elson R C, Selverston A I, Huerta R, Rulkov N F, Rabinovich M I and Abarbanel H D I 1998 *Phys. Rev. Lett.* **81** 5692
[12] Bao B C, Hu A H, Xu Q, Bao H, Wu H G and Chen M 2018 *Nonlinear Dyn.* **92** 1695
[13] Bao H, Hu A H and Liu W B 2019 *Int. J. Bifurc. Chaos* **29** 1950006
[14] Ge M Y, Jia Y, Xu Y and Yang L J 2018 *Nonlinear Dyn.* **91** 515

[15] Parastesh F, Rajagopal K, Karthikeyan A, Alsaedi A, Hayat T and Pham V T 2018 *Cogn. Neurodyn.* **12** 607
[16] Lv M and Ma J 2016 *Neurocomputing* **205** 375
[17] Qu L H, Du L, Deng Z C, Cao Z L and Hu H W 2018 *Chin. Phys. B* **27** 118707
[18] Yuan Z X, Feng P H, Du M M and Wu Y 2020 *Chin. Phys. B* **29** 030504
[19] Lv M, Wang C N, Ren G D, Ma J and Song X L 2016 *Nonlinear Dyn.* **85** 1479
[20] An X L and Qiao S 2021 *Chaos Solitons Fractals* **143** 110587
[21] Ma J and Tang J 2017 *Nonlinear Dyn.* **89** 1569
[22] Carpenter C J 1999 *IEE Proceedings-Science, Measur. Technol.* **146** 182
[23] Chua L O 2015 *Radioengineering* **24** 319
[24] Xu Q, Lin Y, Bao B C and Chen M 2016 *Chaos Solitons Fractals* **83** 186
[25] Wu F Q, Wang C N, Xu Y and Ma J 2016 *Sci. Rep.* **6** 28
[26] Ma J and Tang J 2017 *Nonlinear Dyn.* **89** 1569
[27] Yu F, Zhang Z N, Shen H, Huang Y Y, Cai S, Jin J and Du S C 2021 *Front. Phys.* **9** 690651
[28] Kafraj M S, Parastesh F and Jafari S 2020 *Chaos Solitons Fractals* **137** 109782
[29] Wang Y, Ma J, Xu Y, Wu F Q and Zhou P 2017 *Int. J. Bifurc. Chaos* **27** 1750030
[30] Jin W Y, Wang A, Ma J and Lin Q 2019 *Sci. China Technol. Sci.* **62** 2113
[31] Ge M Y, Jia Y, Xu Y and Yang L J 2018 *Nonlinear Dyn.* **91** 515
[32] Qu L H, Du L, Hu H W, Cao Z L and Deng Z C 2020 *Nonlinear Dyn.* **102** 2739
[33] Gu H G, Pan B B and Li Y Y 2015 *Nonlinear Dyn.* **82** 1191
[34] Bao H, Hu A H, Liu W B and Bao B C 2020 *IEEE Trans. Neural Netw. Learning Sys.* **31** 502
[35] Lin H R, Wang C H, Sun Y C and Yao W 2020 *Nonlinear Dyn.* **100** 3667
[36] Bao H, Liu W B and Hu A H 2019 *Nonlinear Dyn.* **95** 43
[37] Marco M D, Forti M and Pancioni L 2017 *IEEE Trans. Cybernetics* **47** 2970
[38] Lai Q, Hu B, Guan Z H, Li T, Zheng D F and Wu Y H 2016 *Neurocomputing* **207** 785
[39] Tang Y X, Khalaf A J M, Rajagopal K, Pham V T, Jafari S and Tian Y 2018 *Chin. Phys. B* **27** 040502
[40] Li C B, Xu Y J, Chen G R, Liu Y J and Zheng J C 2019 *Nonlinear Dyn.* **95** 1245
[41] Yu F, Qian S, Chen X, Huang Y Y, Cai S, Jin J and Du S C 2021 *Complexity* **2021** 6683284
[42] Bao H, Liu W B and Chen M 2019 *Nonlinear Dyn.* **96** 1879
[43] Rulkov N F 2002 *Phys. Rev. E* **65** 041922
[44] Wang G H, Peng M S, Zuo J and Cheng R R 2017 *Nonlinear Dyn.* **89** 2553
[45] Li D, Zheng Y and Yang Y 2019 *Indian J. Phys.* **93** 1477
[46] Bashkirtseva I, Nasyrova V and Ryashko L 2020 *Int. J. Bifurc. Chaos* **30** 2050153
[47] Bashkirtseva I, Nasyrova V and Ryashko L 2018 *Chaos Soliton Fractals* **110** 76
[48] Wang C X and Cao H J 2015 *Commun. Nonlinear Sci. Numer. Simulat.* **20** 536
[49] Sun H J and Cao H J 2016 *Commun. Nonlinear Sci. Numer. Simulat.* **40** 15
[50] Budzinski R C, Lopes S R and Masoller C 2021 *Neurocomputing* **1** 44
[51] Sarbendu R, Arnob R, Bera B K and Dibakar G 2018 *Nonlinear Dyn.* **94** 785
[52] Xu Q, Song Z, Bao H, Chen M and Bao B C 2018 *AEU-Int. J. Electron. Commun.* **96** 66
[53] Xu W, Wang Y Q, Li Y F, Gao F, Zhang M C, Lian X J, Wan X, Xiao J and Tong Y 2019 *Acta Phys. Sin.* **68** 238501 (in Chinese)
[54] Chen J C, Chen J Q, Bao H, Chen M and Bao B C 2018 *Nonlinear Dyn.* **95** 3385
[55] Wolf A, Swift J B, Swinney H L and Vastano J A 1985 *Physica D* **16** 285
[56] Bao B C, Xu Q, Bao H and Chen M 2016 *Electron. Lett.* **52** 1008
[57] Bao H, Chen M, Wu H G and Bao B C 2020 *Sci. China Tech. Sci.* **63** 603
[58] Jafari S, Ahmadi A, Khalaf A, Abdolmohammadi H R, Pham V T and Alsaadi F E 2018 *Int. J. Electron. Commun. (AEÜ)* **89** 131
[59] Yuan F, Wang G Y, Shen Y R and Wang X Y 2016 *Nonlinear Dyn.* **86** 37
[60] Bao B C, Zhu Y X, Ma J, Bao H, Wu H G and Chen M 2021 *Sci. China Tech. Sci.* **64** 1107